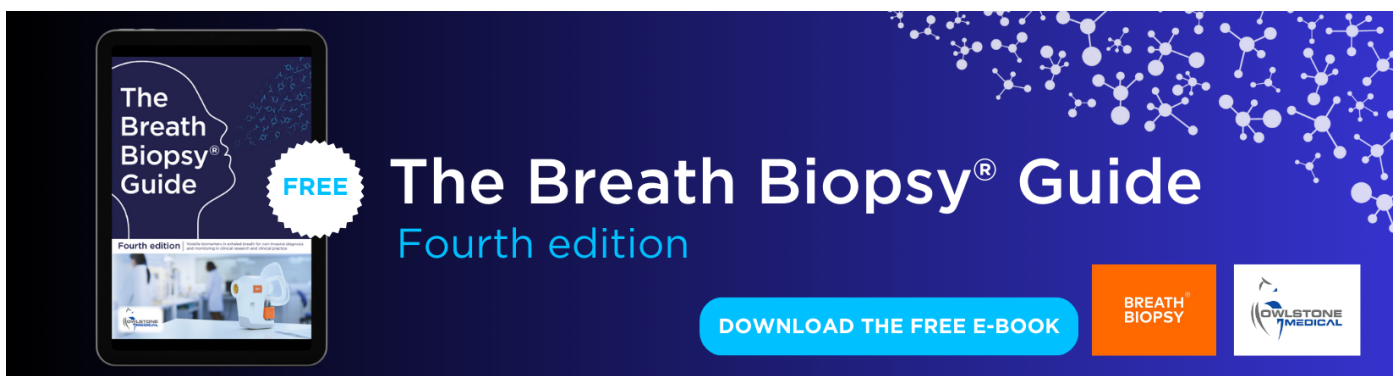**PAPER • OPEN ACCESS**

A probabilistic transcranial magnetic stimulation localization method

To cite this article: Juhani Kataja *et al* 2021 *J. Neural Eng.* **18** 0460f3

View the article online for updates and enhancements.

Journal of Neural Engineering

PAPER

A probabilistic transcranial magnetic stimulation localization method

Juhani Kataja[1,*] , Marco Soldati[1] , Noora Matilainen[1] and Ilkka Laakso[1,2]

[1] Department of Electrical Engineering and Automation, Aalto University, Espoo, Finland
[2] Aalto Neuroimaging, Aalto University, Espoo, Finland
* Author to whom any correspondence should be addressed.

E-mail: juhani.m.kataja@aalto.fi

Abstract

Objective. Transcranial magnetic stimulation (TMS) can be used to safely and noninvasively activate brain tissue. However, the characteristic parameters of the neuronal activation have been largely unclear. In this work, we propose a novel neuronal activation model and develop a method to infer its parameters from measured motor evoked potential signals. *Approach.* The connection between neuronal activation due to an induced electric field and a measured motor threshold is modeled. The posterior distribution of the model parameters are inferred from measurement data using Bayes' formula. The measurements are the active motor thresholds obtained with multiple stimulating coil locations, and the parameters of the model are the location, preferred direction of activation, and threshold electric field value of the activation site. The posterior distribution is sampled using a Markov chain Monte Carlo method. We quantify the plausibility of the model by calculating the marginal likelihood of the measured thresholds. The method is validated with synthetic data and applied to motor threshold measurements from the first dorsal interosseus muscle in five healthy participants. *Main results.* The method produces a probability distribution for the activation location, from which a minimal volume where the activation occurs with 95% probability can be derived. For eight or nine stimulating coil locations, the smallest such a volume obtained was approximately 100 mm^3. The 95% probability volume intersected the pre-central gyral crown and the anterior wall of the central sulcus, and the preferred direction was perpendicular to the central sulcus, both findings being consistent with the literature. Furthermore, it was not possible to rule out if the activation occurred either in the white or grey matter. In one participant, two distinct activations sites were found while others exhibited a unique site. *Significance.* The method is both generic and robust, and it lays a foundation for a framework that enables accurate analysis and characterization of TMS activation mechanisms.

1. Introduction

Transcranial magnetic stimulation (TMS) is a non-invasive electromagnetic brain stimulation technique relying on generation of electromotive force in the brain with a time-varying magnetic flux density. Variants of TMS have been shown to have promising levels of therapeutic utility to numerous neurological and psychiatric conditions [1, 2].

TMS is also used as a cortical mapping tool [1, 3]. In TMS neuronavigation, the position of the magnetic coil is tracked in real time, which allows to relate evoked electrophysiological responses to a spatial location [4]. In conventional projection-based approaches, the activation site is taken to be directly under the coil location that produces the largest motor-evoked potential (MEP) amplitudes. However, the electric field induced in the brain is spatially diffuse, and hence, sites at some distance from the center of the magnetic coil can also be activated. This makes it difficult to precisely locate the activated neuronal structures. The induced electric field is

affected by anatomical features, such as the individual anatomy of the gyri and sulci [5, 6]. Hence, anatomically realistic computational models are needed to improve the localization of the TMS activation site(s) [6, 7].

Several methods that use induced electric field models for localizing the TMS activation site in the primary motor cortex have been previously investigated. These methods are based on an assumption that there is a unique localized activation site. The generation of the physiological responses is explained by the strength and/or direction of the induced electric field at that site [8]. Hence, applying TMS at multiple locations over the scalp, measuring the MEP signals, and calculating the induced electric fields produce data that can be used to determine the location of the activation site. It should be noted that other cortical sites are probably activated at the same time, but their activation is not assumed to contribute to the measured signals. By applying a single activation site model, [8] proposed that the activation site is found where the variance of the electric field across stimulating coil configurations is minimized. They utilized a spherical model of the cortex and solved the total quasi-static electric field in it [8]. Similarly, [7] found the sites where the norm of electric field or its normal component to cortical surface varied the least across coil configurations, but in their work, a finite element model of the cortex was used. A similar approach based on the single-site activation model was proposed by [9]. Others have proposed techniques based on, e.g. weighted averaging of the electric field based on the strength of the evoked motor responses [5, 6, 10].

Recently, [11] discussed an approach of approximating a certain sigmoidal type functions, parametrized by location r, of the form $\vec{E}(r) \mapsto \mathrm{MEP}_r(\vec{E}(r))$, where $\vec{E}(r)$ is the electric field at location r and $\mathrm{MEP}_r(\bullet)$ is the amplitude of the MEP given electric field, and proposing the site where these functions overlap, when the coil configuration is varied, to be the most plausible location of MEP eliciting activation site. In addition, they conclude, using permutation analysis, that 6 out of 20 coil configurations provided largely the same information content as the measurements with all 20 coil configurations [11].

The main drawback of these previous methods is that the cortical activation models are not spelled out explicitly. Furthermore, the activation sites are inferred from maximizing the value of some correlation-type measures, and quantitative measures indicating how well the proposed, albeit implicit, cortical localization model supports the measured data are not provided.

The present work contributes to development of TMS mapping methods addressing these issues in a probabilistic setting using a physiologically plausible single-site activation model: an activation in the cerebrum occurs if some component of the stimulating electric fields exceeds a certain threshold value. The model parameters are inferred from the measured motor thresholds (MTs) using Bayes' formula. In addition, numerical techniques are presented to calculate the emerging integrals.

The end results of the method are certain posterior density functions of the model parameters and statistics associated to those densities given measured MT values. We analyze MTs measured with five participants using the method, and further validate it with synthetic MTs generated with the activation model.

The rest of the paper is organized as follows. The theoretical background of the method is presented in section 2. In section 2.1, we briefly detail on how the required electric fields in the brain are simulated. The localization method together with details of the cortical activation model itself is presented in section 2.2 and in the following sections. In section 3, we describe in detail the setup used to measure the MTs of the participants, and in section 4, the present method is used to analyze MTs of the five participants.

2. Model

2.1. Stimulation field model

We stimulate the brain with a monophasic magnetic pulse, which will result in a primary magnetic flux density $\vec{B}_p = \mathrm{curl}\,\vec{A}_p$ in the brain having a reasonably fast rise time rendering the model proposed by [12] applicable. Thus, the total electric field in the brain is given by $\vec{E} = -\mathrm{grad}\,\phi - \frac{\partial}{\partial t}\vec{A}_p$ where $\mathrm{div}\,\sigma\vec{E} = 0$, and so ϕ is the unique function (up to a constant) in $H^1(D_{\mathrm{brain}})$, $D_{\mathrm{brain}} \subset \mathbb{R}^3$, that satisfies

$$\int_{D_{\mathrm{brain}}} \mathrm{grad}\,\psi \cdot \sigma\,\mathrm{grad}\,\phi\,dx = -\int_{D_{\mathrm{brain}}} \mathrm{grad}\,\psi \cdot \frac{\partial}{\partial t}\vec{A}_p dx,$$
$$\forall \psi \in H^1(D_{\mathrm{brain}}), \qquad (1)$$

where σ is the tissue conductivity and $H^1(D_{\mathrm{brain}})$ is the Sobolev space consisting of square integrable functions in D_{brain}, with square integrable weak gradients. For notation and mathematical details we refer to any text book on finite elements such as the one by [13].

We solve (1) using a multi-grid based finite element method developed in [14] with 0.5 mm trilinear cubic elements and the exciting vector potential $\vec{A}_p$ is that of the figure-of-eight coil in [15]. The conductivity data for the finite element solver was inferred from MR images such a way that various tissues are given isotropic homogeneous conductivity values shown in table 1, section 3.2. The electric field is interpolated at the center of each element and voxelized as an element-wise constant function.

2.2. Localization model

Our approach expands upon the single-site activation model [8]. We assume that there is a location in the

cerebrum, a preferred direction, and a threshold magnitude, denoted by $\boldsymbol{r}$, $\vec{d}$ and E_{thr}, respectively, which are responsible for the observed MEP in a following way: The probability of a MEP being elicited at $\boldsymbol{r}$ is a monotonously increasing function w.r.t. $\vec{d} \cdot \vec{E}(\boldsymbol{r})$ reaching 0.5 when $\vec{d} \cdot \vec{E}(\boldsymbol{r}) = E_{\text{thr}}$.

Now, given the activation site parameters $\vec{d}$, $\boldsymbol{r}$ and E_{thr}, the MT associated with a coil configuration k, denoted by t_k, is defined by

$$t_k = \frac{E_{\text{thr}}}{\vec{E}_k(\boldsymbol{r}) \cdot \vec{d}}, \qquad (2)$$

where $\vec{E}_k$ is the total induced electric field due the coil configuration k at the maximum stimulator intensity setting.

The rationale of such a definition is that when the stimulator intensity passes t_k the MEP probability increases quickly allowing us to infer an approximate value for t_k from the electromyography (EMG) measurements.

From prior knowledge [16, 17], E_{thr} is bounded from below at the scale of 100 V m^{-1}. We chose $E_{\text{thr}} > 60 \text{ V m}^{-1} = E_{\text{thr,prior}}$, where the lower bound is deliberately chosen to impose as little prior belief as plausible. Finally, combining E_{thr} and $\vec{d}$ to $\boldsymbol{s} = \frac{\vec{d}}{E_{\text{thr}}}$, we arrive at the model that connects activation site, direction and threshold with minimal activation eliciting stimulation setting t_k:

$$t_k = \frac{1}{\vec{E}_k(\boldsymbol{r}) \cdot \boldsymbol{s}}. \qquad (3)$$

However, because t_k is inferred from noisy measurements, we model t_k, $\boldsymbol{r}$ and $\boldsymbol{s}$ as random variables, denoted by T_k, R, and S, respectively, and replace (3) with a multiplicative noise model

$$T_k = \frac{1}{\vec{E}_k(R) \cdot S}(1 + Kn), \qquad (4)$$

where $n \sim \mathcal{N}(0,1)$ and $K > 0$ is a noise parameter, typically $K = \frac{1}{20}$. Such an approach is often utilized in probabilistic methods in inverse problems [18].

The rationale of such a model is based on an experimental observation that the active motor threshold (aMT) values associated with higher intensity stimulus settings tend to vary more.

Thus, the likelihood distribution of T_k given $\boldsymbol{r}$ and $\boldsymbol{s}$ is

$$\pi(t_k|\boldsymbol{r},\boldsymbol{s}) = \frac{|\vec{E}_k(\boldsymbol{r}) \cdot \boldsymbol{s}|}{\sqrt{2\pi}K} e^{-\frac{1}{2K^2} \|t_k \vec{E}_k(\boldsymbol{r})\boldsymbol{s}-1\|^2}$$

and joint likelihood distribution of N coil configurations, denoting $\boldsymbol{t} = [t_1, \ldots, t_N]$, $\mathbf{T} = \text{diag}(t_1, \ldots, t_N)$, and $\mathbf{E}(\boldsymbol{r}) = [\vec{E}_1(\boldsymbol{r}), \vec{E}_2(\boldsymbol{r}), \ldots, \vec{E}_N(\boldsymbol{r})]^{\text{T}} \in \mathbb{R}^{N\times 3}$, is given by
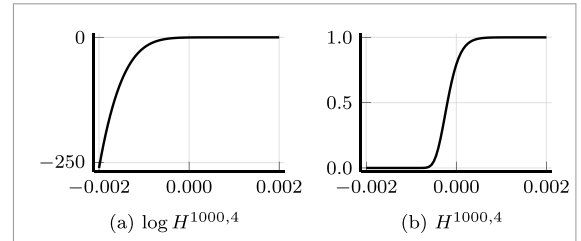
Figure 1. A smooth step functions defined by equation (7).

$$\pi(\boldsymbol{t}|\boldsymbol{r},\boldsymbol{s}) = \frac{\Pi_{k=1}^{N}|\vec{E}_k(\boldsymbol{r}) \cdot \boldsymbol{s}|}{(\sqrt{2\pi}K)^N} e^{-\frac{1}{2K^2} \|\mathbf{TE}(\boldsymbol{r})\boldsymbol{s}-1\|^2}. \qquad (5)$$

The prior distribution of S is chosen as follows

$$\pi_S(\boldsymbol{s}) \propto q_S(\boldsymbol{s}) = H^{\kappa,\nu}\left(\frac{1}{E_{\text{thr,prior}}} - |\boldsymbol{s}|\right), \qquad (6)$$

where $H^{\kappa,\nu}$ is a smoothed step function with parameters κ and ν determining the approximation error to the step function. This step function is defined by

$$\log H^{\kappa,\nu}(x) = -\left(\log(1 + e^{-2\kappa x})\right)^{\nu}, \qquad (7)$$

and for numerical stability we use the asymptotic $-(2\kappa x)^{\nu}$, when $2\kappa x < -10$. In actual computations we use the values $\kappa = 10^3$ and $\nu = 4$ which result in a step function graphed in figure 1. Thus, the log-prior function $\log q_S$ acts as a penalty term in the posterior log-probability density when $|\boldsymbol{s}| > \frac{1}{E_{\text{thr,prior}}}$ and the prior function q_S is a very good L_1 estimate of the characteristic function of the set $\{\boldsymbol{s} : |\boldsymbol{s}| < \frac{1}{E_{\text{thr,prior}}}\}$.

The prior distribution of R is proportional to the characteristic function of the set

$$D_R := \bigcap_{k=1\ldots N} \{\boldsymbol{r} \in D_0 : \alpha_k|\vec{E}_k(\boldsymbol{r})| > E_{\text{thr,prior}}\}, \qquad (8)$$

where $\alpha_k > 1$ is big enough of a stimulator intensity value that a MEP occurs certainly and D_0 is the intersection of the precentral gyrus, including both grey and white matter, and a 5 cm ball centered at $[-40.7, -15.7, 59.7]$ in Montreal Neurological Institute (MNI) coordinates [19]. While analyzing the measurements, we chose $\alpha_k = 1.2 t_k$.

Combining the likelihood (5) and priors we arrive, by Bayes' formula, to the log-posterior density up to an additive constant:

$$\log q(\boldsymbol{r},\boldsymbol{s},\boldsymbol{t}) = -\frac{1}{2K^2}\|\mathbf{TE}(\boldsymbol{r})\boldsymbol{s} - 1\|^2$$
$$+ \sum_{k=1}^{N} \log|\vec{E}_k(\boldsymbol{r}) \cdot \boldsymbol{s}| - N\log\left(\sqrt{2\pi}K\right)$$
$$+ \log \pi_S(\boldsymbol{s}). \qquad (9)$$

Thus $\pi(\boldsymbol{r},\boldsymbol{s}|\boldsymbol{t}) \propto q(\boldsymbol{r},\boldsymbol{s},\boldsymbol{t})$.

Let us associate certain *singular value coordinates* with the matrix **TE** as follows. Let the singular value decomposition of **TE** be written as

$$\mathbf{TE} = \sum_{i=1}^{3} \sigma_i \boldsymbol{u}_i \boldsymbol{v}_i^{\mathrm{T}}, \qquad (10)$$

where the singular values $\sigma_i > 0$ are in a descending order. Then the i:th singular value coordinate of $\boldsymbol{s} \in \mathbb{R}^3$ with respect to **TE** is given by $\boldsymbol{s} \cdot \boldsymbol{v}_i$. The value of such a coordinate system is that the posterior distribution $\pi(\boldsymbol{s}|\boldsymbol{r},\boldsymbol{t})$ has a special form in those coordinates as visible in figure 9.

To identify the likely activation sites and the preferred direction of activation, we are interested in the marginal distribution $\pi(\boldsymbol{r}|\boldsymbol{t}) \propto \int q(\boldsymbol{r},\boldsymbol{s},\boldsymbol{t}) \mathrm{d}\boldsymbol{s}$ and the conditional expectation $\mathbb{E}[\boldsymbol{s}|\boldsymbol{r},\boldsymbol{t}]$. The latter can be approximated from the Markov chain Monte Carlo (MCMC) samples immediately, but the marginal distribution calls for computing a normalizing constant which we calculate using path sampling [20].

We review the path sampling method for our case in the following section 2.3.

2.3. Calculation of the marginal distribution

Path sampling allows us to calculate $\pi(\boldsymbol{r}|\boldsymbol{t})$ up to an unknown constant not depending on $\boldsymbol{r}$ or $\boldsymbol{t}$. Denoting the so calculated quantity by $Q(\boldsymbol{r},\boldsymbol{t})$ we find that $\pi(\boldsymbol{r}|\boldsymbol{t}) = \frac{1}{\int Q(\boldsymbol{r},\boldsymbol{t})\mathrm{d}\boldsymbol{r}} Q(\boldsymbol{r},\boldsymbol{t})$.

Let us introduce, in the spirit of the path sampling method, a family of functions $\{q_\lambda(\boldsymbol{r},\boldsymbol{s},\boldsymbol{t})\}_{\lambda \in [0,1]}$ so that q_0 does not depend on $\boldsymbol{r}$ nor $\boldsymbol{t}$ and that $\log q_1$ coincides with (9). Furthermore, let us denote $z(\lambda;\boldsymbol{r},\boldsymbol{t}) = \int q_\lambda(\boldsymbol{r},\boldsymbol{s},\boldsymbol{t})\mathrm{d}\boldsymbol{s}$.

Recall that the path sampling method is based on the following observation [20]:

$$\frac{d}{d\lambda}\log z(\lambda;\boldsymbol{r},\boldsymbol{t}) = \mathbb{E}\left[\frac{d\log q_\lambda(\boldsymbol{s})}{d\lambda}\right], \qquad (11)$$

where the expectation is taken over the distribution $\pi_\lambda(\boldsymbol{s}|\boldsymbol{r},\boldsymbol{t}) \propto q_\lambda(\boldsymbol{r},\boldsymbol{s},\boldsymbol{t})$.

Thus

$$z(1;\boldsymbol{r},\boldsymbol{t}) = z(0;\boldsymbol{r},\boldsymbol{t})$$
$$\times \exp\left\{\int_0^1 \mathbb{E}\left[\frac{d\log q_\lambda(\boldsymbol{r},\boldsymbol{s},\boldsymbol{t})}{d\lambda}\right]d\lambda\right\}, \qquad (12)$$

and

$$Q(\boldsymbol{r},\boldsymbol{t}) = \exp\left\{\int_0^1 \mathbb{E}\left[\frac{d\log q_\lambda(\boldsymbol{s})}{d\lambda}\right]d\lambda\right\} \qquad (13)$$

is the quantity that can be computed with the path sampling method, assuming that $z(0;\boldsymbol{r},\boldsymbol{t})$ is a constant function with respect to $\boldsymbol{r}$ and $\boldsymbol{t}$.
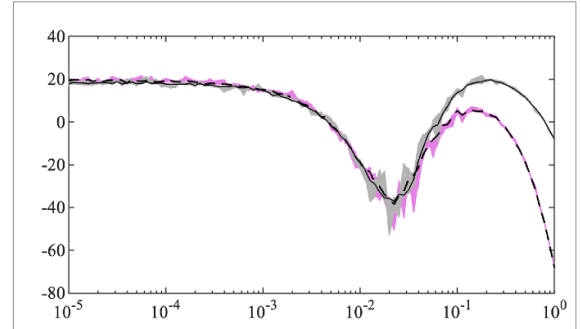

Figure 2. The expectation function $\lambda \mapsto \mathbb{E}[d\log q_\lambda/d\lambda]$ defined in equation (11) with respect to increasing MCMC samples for each value of λ. Black solid: an expectation function associated with a high activation site probability with 1000 MCMC samples. Black dashed: an expectation function associated with a low probability with 1000 samples. Gray and magenta: the same functions with $100 \ldots 1000$ samples.

In our method we chose

$$\log q_\lambda(\boldsymbol{r},\boldsymbol{s},\boldsymbol{t}) = -\frac{\lambda^2}{2K^2}\|\mathbf{TE}(\boldsymbol{r})\boldsymbol{s} - 1\|^2$$
$$+ \lambda \sum_{k=1}^{N} \log|\vec{E}_k(\boldsymbol{r}) \cdot \boldsymbol{s}|$$
$$- \lambda N\log\left(\sqrt{2\pi}K\right) + \lambda^4 \log\pi_S(\boldsymbol{s})$$
$$- (1-\lambda)^2 \frac{1}{2}\left(\frac{E_{\mathrm{thr,prior}}}{0.35}\right)^2 |\boldsymbol{s}|^2. \quad (14)$$

Setting $\lambda = 0$ we observe from the last line of (14), that the resulting log density is roughly proportional to that of normal distribution with standard deviation $\frac{E_{\mathrm{thr,prior}}}{0.35}$, thus $z(0;\boldsymbol{r},\boldsymbol{t}) = \left(\frac{\sqrt{2\pi}0.35}{E_{\mathrm{thr,prior}}}\right)^3$.

The integral (12) is approximated with the trapezoidal quadrature rule having nodes at $(10^{-k})_{k=0,1,\ldots,4}$. The expectation is simulated with a No U-Turns Markov chain Monte Carlo (NUTS MCMC) sampler [21] implemented in AdvancedHMC Julia package [22]. We chose to use, after careful experimentation, 200 adaptation steps and 1000 sampling steps.

Typically, the expectation in (11) as a function of λ resembles the functions displayed in figure 2. Here, most of the integral mass is located at $\lambda > 10^{-1}$ where the integrand is mostly well calculated and when $\lambda < 10^{-1}$, the integrand is bounded from below. From the figure 2 we conclude that the value of the expectation function is quite well approximated with only 1000 MCMC samples for each value of λ as the gray and magenta shades obtained with $100 \ldots 1000$ samples per value of λ enclose quite tightly enclose graphs with 1000 samples.

2.4. Evaluation of model quality

The marginal likelihood (MLH) $p(\boldsymbol{t})$ of the threshold values assuming the proposed model is correct is given by the integral

$$p(\boldsymbol{t}) = \int \pi(\boldsymbol{t}|\boldsymbol{r},\boldsymbol{s})\pi_R(\boldsymbol{r})\pi_S(\boldsymbol{s})\mathrm{d}\boldsymbol{r}\mathrm{d}\boldsymbol{s}. \qquad (15)$$

The integral on the right hand side has an expression in terms of $Q(\boldsymbol{r},\boldsymbol{t})$ and $z(0;\boldsymbol{r},\boldsymbol{t})$:

$$\int \pi(\boldsymbol{t}|\boldsymbol{r},\boldsymbol{s})\pi_R(\boldsymbol{r})\pi_S(\boldsymbol{s})\mathrm{d}\boldsymbol{r}\mathrm{d}\boldsymbol{s}$$

$$= \frac{1}{\underbrace{\int q_S(\boldsymbol{s})\mathrm{d}\boldsymbol{s}}_{=I_S}|D_R|}\int q_1(\boldsymbol{r},\boldsymbol{s},\boldsymbol{t})\mathrm{d}\boldsymbol{r}\mathrm{d}\boldsymbol{s}$$

$$= \frac{1}{I_S|D_R|}\int z(1;\boldsymbol{r},\boldsymbol{t})\mathrm{d}\boldsymbol{r}$$

$$= \frac{1}{I_S|D_R|}\int z(0;\boldsymbol{r},\boldsymbol{t})Q(\boldsymbol{r},\boldsymbol{t})\mathrm{d}\boldsymbol{r}, \qquad (16)$$

where we denote the volume of D_R by $|D_R|$. However, due to discretization, we actually approximate integrals over $\boldsymbol{r}$ variable as sums over the voxels multiplied by their volumes.

The quantity under the last integrand in (16) is the normalizing constant $z(1;\boldsymbol{r},\boldsymbol{t})$ whose small values indicate that the data does not fit very well with the model for the given site $\boldsymbol{r}$.

This quantity has utility in evaluating the quality of the localization. In particular, a small MLH suggests that the measured data is inconsistent with the single-site activation model, e.g. if one or more of the measured aMT are related to a different activation site.

We also calculate leave-one-out cross-validation (CV) measures of the predicted MTs as follows. Let $\boldsymbol{r}_k^* = \mathrm{argmax}_{\boldsymbol{r}} \pi(\boldsymbol{r}|t_1,\ldots,t_{k-1},t_{k+1},\ldots,t_N)$ and $\boldsymbol{s}_k^* = \mathbb{E}(S|\boldsymbol{r}_k^*,t_1,\ldots,t_{k-1},t_{k+1},\ldots,t_N)$ be estimates of $\boldsymbol{r}$ and $\boldsymbol{s}$ with k:th measurement left out. Then the predicted MT is defined by

$$t_k^* = \frac{1}{\boldsymbol{s}_k^* \cdot \vec{E}_k(\boldsymbol{r}_k^*)}, \qquad (17)$$

and the root-mean-square error of CV predictions to measured MTs is given by

$$CV = \sqrt{\frac{1}{N}\sum_{k=1}^{N}\left(\frac{|t_k - t_k^*|}{t_k}\right)^2}. \qquad (18)$$

The additional utility of CV measures is that it shows if a subset of measurements can predict the measured MT that is not used in calculating the model estimates $\boldsymbol{r}_k^*$ and $\boldsymbol{s}_k^*$.

2.5. Generation of synthetic data

For validation purposes we shall generate *synthetic thresholds*, denoted by $t_{k,\mathrm{syn}}$, as follows: Let $\boldsymbol{s}_{\mathrm{syn}} \in \mathbb{R}^3$ be s.t. $|\boldsymbol{s}_{\mathrm{syn}}| < \frac{1}{E_{\mathrm{thr,prior}}}$ and $\boldsymbol{r}_{\mathrm{syn}} \in D_0$ and let $(\vec{E}_k)_{k=1}^{N}$ be the induced electric field associated with $k =$

$1\ldots N$ coil locations. Then $t_{k,\mathrm{syn}}$ is obtained by plugging these values to (3):

$$t_{k,\mathrm{syn}} = \frac{1}{\boldsymbol{s}_{\mathrm{syn}} \cdot \vec{E}_k(\boldsymbol{r}_{\mathrm{syn}})}. \qquad (19)$$

We define a random variable based on the noise model in (4):

$$T_{k,\mathrm{syn}} = t_{k,\mathrm{syn}}(1 + Kn), \qquad (20)$$

where $n \sim \mathcal{N}(0,1)$, and $K = \frac{1}{20}$.

Drawing samples from $T_{k,\mathrm{syn}}$ we can generate *virtual measurements* and we can attempt to locate the previously selected synthetic activation site. Furthermore, using these synthetic thresholds, we can provide ball-park figures for the MLH values because the virtual measurements are consistent with the single-site activation model by definition. By drawing multiple virtual measurements ($n = 30$), we can define an empirical quantile function for MLH, denoted by $\mathcal{K}(p(\tilde{t}_{1,\mathrm{syn}},\ldots,\tilde{t}_{N,\mathrm{syn}});N)$, or just $\mathcal{K}$ for short, corresponding to number of coil locations N and sampled thresholds $\tilde{t}_{1,\mathrm{syn}},\ldots,\tilde{t}_{N,\mathrm{syn}}$.

In section 4.1 we present localization results based on synthetic thresholds and virtual measurements.

The numerical values of $\boldsymbol{r}_{\mathrm{syn}}$ and $|\boldsymbol{s}_{\mathrm{syn}}|^{-1}$ were chosen to be $[-37.3, -18.6, 65.7]$ in MNI coordinates [7], and 65 V m^{-1}, respectively. The direction of $\boldsymbol{s}_{\mathrm{syn}}$ was chosen to be in the posterior-anterior direction roughly normal to central sulcus and scalp.

2.6. Model statistics

The key localization statistic calculated from the posterior distribution is the *95% probability volume*, denoted here by $V_{0.95}$. It is defined to be the smallest set of voxels, in terms of volume, that satisfies

$$\int_{V_{0.95}} \pi(\boldsymbol{r}|\boldsymbol{t})\mathrm{d}\boldsymbol{r} \geq 0.95. \qquad (21)$$

Furthermore, we can calculate the maximum *a-posteriori* (MAP) estimate $\boldsymbol{r}_{\mathrm{MAP}}$ of marginal distribution $\pi(\boldsymbol{r}|\boldsymbol{t})$, and the expected values of E_{thr} and $\boldsymbol{s}$ at $\boldsymbol{r}_{\mathrm{MAP}}$.

In order to assess the plausibility of the localization we calculate the MLH value and evaluate the corresponding value of the empirical quantile function $\mathcal{K}$ for an informal *p*-value of the measurements.

3. Experimental methods and pre-processing

3.1. Participants

Seven healthy participants (four male, three female, mean age ± standard deviation = 30 ± 6 years) were recruited for the study. Each of them was requested to provide an informed written consent prior

to participating to the experiment. The study protocol was approved by the bmissions Aalto University Research Ethics committee. All methods were carried out in accordance with approved institutional guidelines and regulations.

A set of structural T1- and T2-weighted magnetic resonance images were acquired with the participants laying in supine position. The parameters used for the acquisitions are reported as follows: T1, TR/TE/TI/FA/FOV/voxel size/slice number = 1800 ms/1.99 ms/800 ms/9°/256 mm/ $1 \times 1 \times 1$ mm/176; T2, TR/TE/FOV/voxel size/slice number = 3200 ms/412 ms/256 mm/ $1 \times 1 \times 1$ mm /176.

One participant was excluded from analysis due to unstable coil location during the experiments and one participant was only used for producing synthetic data. Thus, five participants (three male, two female, mean age ± standard deviation = 29 ± 5 years) were available in the actual analysis.

3.2. Segmentation

FreeSurfer [23, 24] was employed for the reconstruction of white (WM) and grey (GM) matter from the T1-weighted images. The other non-brain tissues (i.e. cerebrospinal fluid (CSF), skin, skull) were segmented through a semi-automatic procedure [25], which makes use of both T1- and T2-weighted images. The obtained segmented images were then voxelized using a uniform grid consisting of cubic voxel with a side length of 0.5 mm. The final volume conductor models were generated by assigning the tissues electrical conductivities to each voxel based on the values reported in table 1. The conductivities of the WM and GM were derived from the values measured at the frequency of 50 kHz [26]. A parametric model [27] was then used to estimate the conductivities at the center frequency of the TMS stimulator (3 kHz). In figure 3 the interfaces of WM-GM, GM-CSF and CSF-skull segmented domains are shown overlaid on top of MR images of three participants.

The individual participants' brain triangulated surfaces were reconstructed using the FreeSurfer software, and the obtained surfaces were mapped to template surfaces similarly reconstructed from the MNI ICBM 2009a nonlinear asymmetric template [28, 29], thus providing us with a mapping from each participant's brain to the standard MNI coordinates.

3.3. Transcranial magnetic stimulation

We used Magstim 200^2 stimulator (Magstim Company, UK) with a figure-of-eight coil having the two loops both 9 cm in diameter. The center of the coil was placed above and around the M1 region of the hand area of the left motor cortex at nine configurations determined in advance based on electric field simulations. One coil location was directly above the hand knob region, $r_{M1} = [-41, -7, 63]$ in MNI coordinates

Table 1. Electrical conductivities of the tissues (mS m^{-1}).

Tissue	Conductivity (mS m^{-1})	Reference
GM	215[b]	[26]
WM	142[b]	[26]
CSF	1790	[30]
Compact bone	9[a]	[31]
Spongy bone	34[a]	[31]
Subcutaneous fat	150	[32]
Skin	430	[32]
Muscle	180	[33]
Blood	700	[34]

[a] Values increased by 30% to compensate room temperature measurements [30, 35, 36].
[b] Values decreased by 17% to compensate for the measurement frequency of 50 kHz by applying the four Cole–Cole model [27].

[9], and the remaining eight locations were placed around the center position at a distance of 2–3 cm. At the center location, the coil direction was chosen so that the calculated induced electric field at r_{M1} was perpendicular to the central sulcus in the posterior-anterior direction. The direction of the coil at other locations was chosen so that the induced electric field direction at r_{M1} was different for each coil location, such that the maximum angle between field directions was 30°. This was achieved by choosing eight equally spaced angles between −15° and +15° and randomly assigning the angles to the coil locations. Electric field simulations were then performed for each coil location to determine the coil orientation that produced the desired deviation from the perpendicular direction. Finally, the pre-determined coil locations and directions were marked on the MR images. The approach produces approximately ±15° variability in the electric field directions, which aids our method to better estimate the preferred direction of activation.

In the experiments, the location of the coil was navigated and recorded with a Visor2 TMS neuronavigation system (ANT Neuro, Enschede, the Netherlands), using the pre-determined coil configurations as a guideline. Figure 4 shows the maximum angle between electric fields based on the realized coil locations and directions. In the same figure, the electric field norm at threshold intensity is also shown together with an activation *a-posteriori* location. As the coil was not placed exactly at the pre-determined locations, the maximum opening angle at r_{M1} can differ from 30°.

The MEPs were recorded from first dorsal interosseus muscle (FDI) with surface EMG electrodes. The participants were requested to lightly squeeze a small object and, by doing so, actively trying to maintain the peak-to-peak amplitude of the EMG signal displayed to them around 200 μV. The EMG signal was sampled at 5 kHz and high- and lowpass filtered to 15 to 500 Hz range for visualization. The EMG
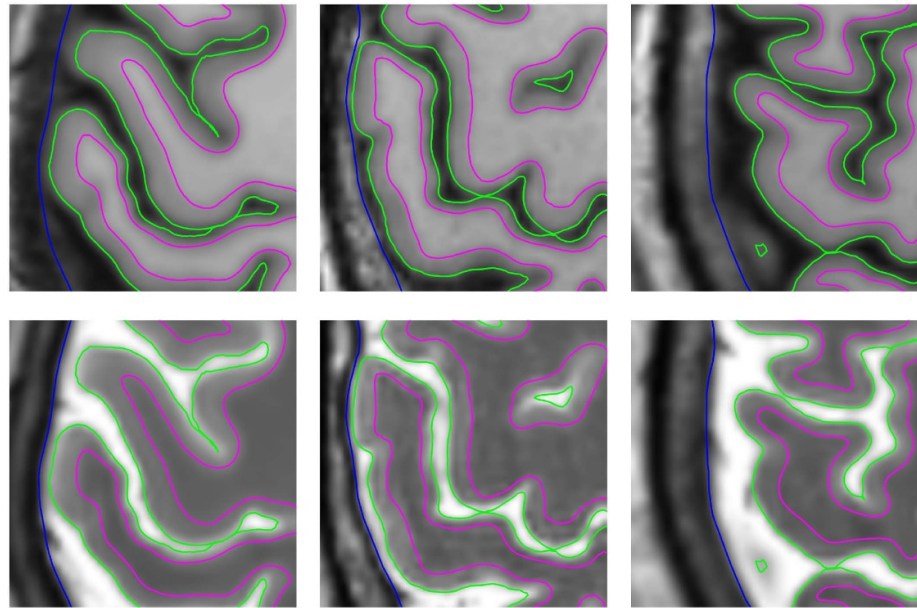
Figure 3. Segmented WM-GM (magenta), GM-CSF (green) and CSF-skull (blue) surfaces overlaid on top of T1-weighted (top) and T2-weighted (bottom) MR images centered around target region. The images are of axial plane slices of participants 1, 2 and 4 (left to right).
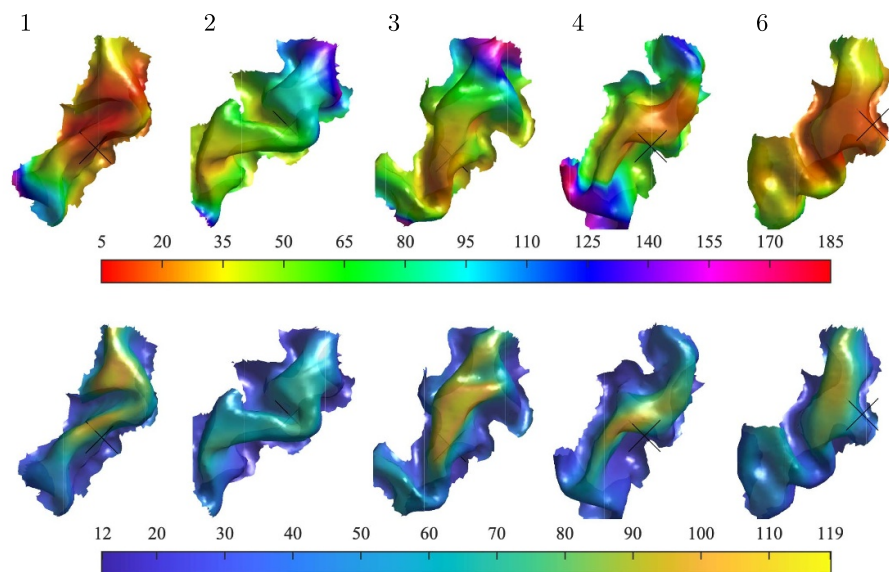

Figure 4. Maximum opening angles in degrees of electric fields arising from all applicable stimulation locations at 2 mm depth in cortex around region of interest (top row). Average electric field in V m^{-1} over coil configurations at aMT stimulus intensity (bottom row). The participant Id is shown on top left side of the map. The hand knob area is visible at the center of the center of the image.

signals were recorded with a NeurOne system (Neur-One, MEGA Electronics Ltd Finland).

During the experiment, the aMTs were scouted by stimulating around ten times at each stimulation intensity with >3 s intervals and visually determining the presence or lack of a MEP.

3.4. Processing of MEP data

After the experiments, the values of the aMT were determined from highpass filtered (10 Hz) EMG signals by finding the lowest intensity for which the amplitude of the first negative phase of the MEP exceeded 100 μV in 50% of the trials.
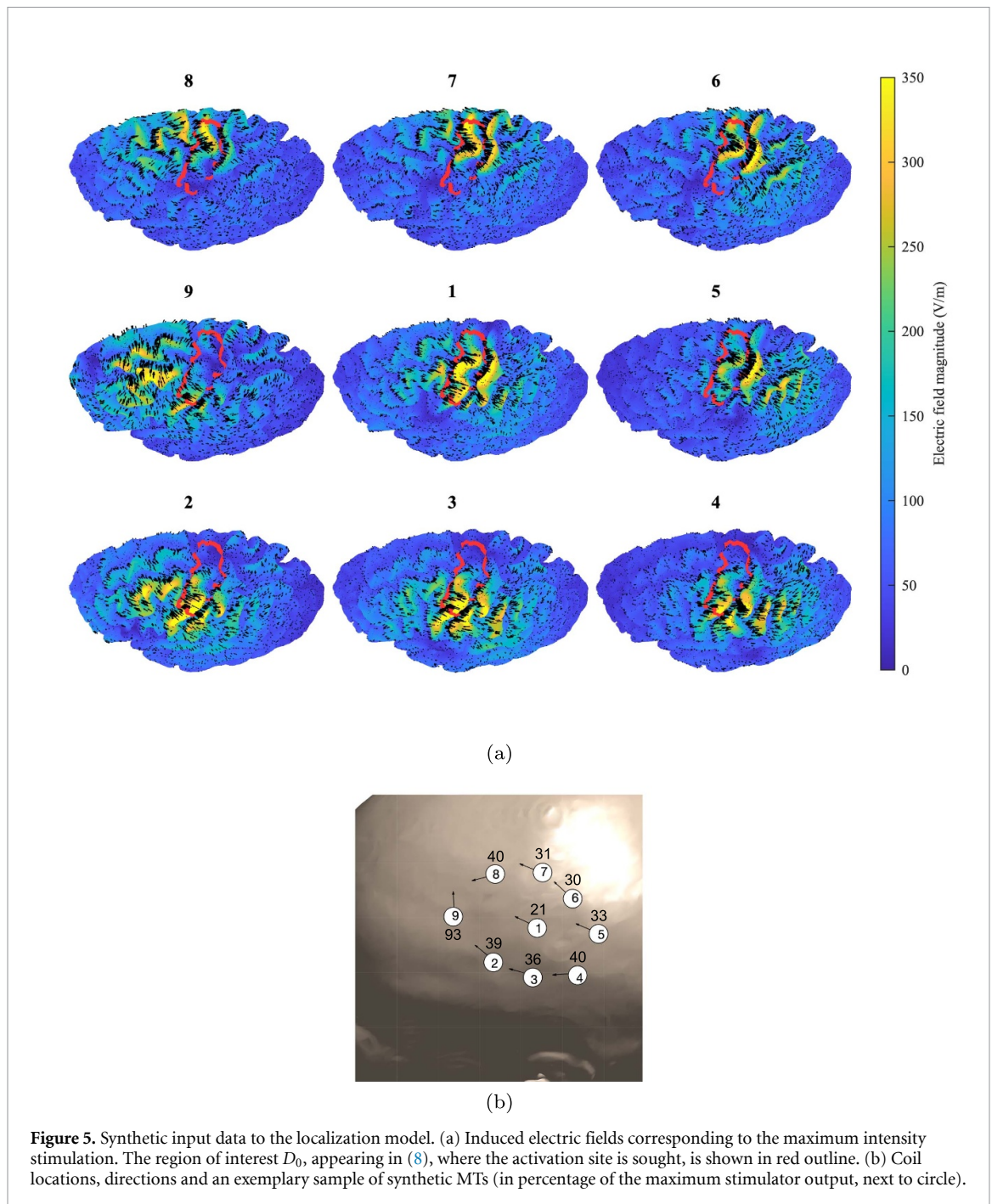
(a)

(b)

Figure 5. Synthetic input data to the localization model. (a) Induced electric fields corresponding to the maximum intensity stimulation. The region of interest D_0, appearing in (8), where the activation site is sought, is shown in red outline. (b) Coil locations, directions and an exemplary sample of synthetic MTs (in percentage of the maximum stimulator output, next to circle).

For visualization of the MEPs, the median of the slightly suprathreshold MEP signals (aMT $\leq$ intensity $\leq$ aMT+3%) was calculated. The MEP signals that did not exceed 100 μV were excluded in this calculation.

4. Results and analysis

4.1. Model validation with synthetic data

The model is in part validated with virtual measurements obtained as samples of the random variable $T_{k,\mathrm{syn}}$ defined in equation (20). The virtual measurements are known to originate from the proposed

activation model and thus the method should successfully localize the activation site, and they also provide values of the MLH against which to compare the MLH values resulting from actual measurements. The electric fields and coil locations used to construct the synthetic measurements are displayed in figure 5.

Drawing 30 samples from each of the random variables $T_{k,\mathrm{syn}}$, $k = 1 \ldots N$, we calculate the maximum *a posteriori* locations $\boldsymbol{r}_{\mathrm{MAP}}$, 95% probability volumes, MLHs, and expected values of E_{thr} and $\boldsymbol{s}$ at the corresponding $\boldsymbol{r}_{\mathrm{MAP}}$. The statistics of these quantities are displayed in figures 6(a)–(c), and the evolution of the 95% probability volume, together
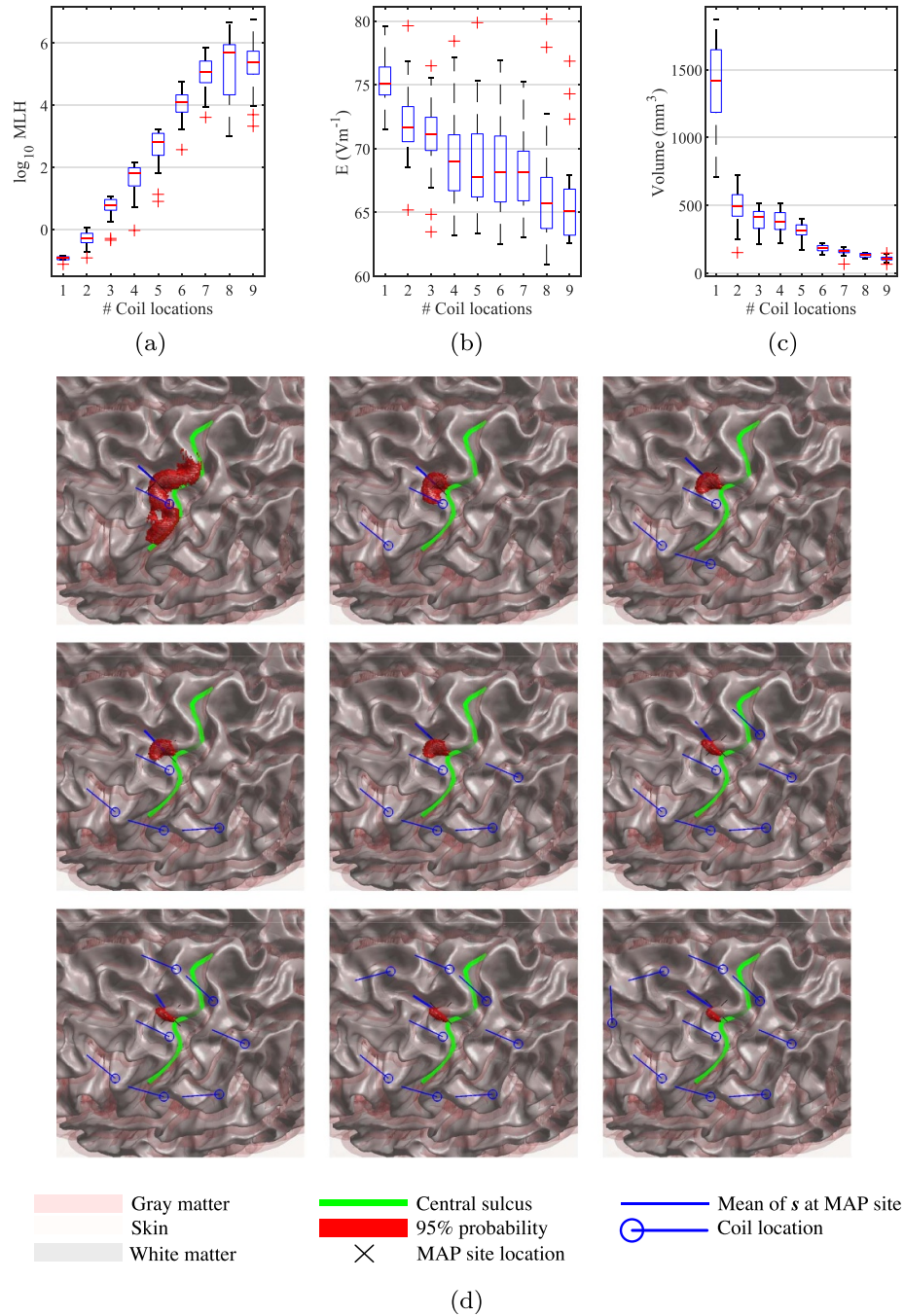
Figure 6. Activation statistics calculated for the synthetic data. (a) Log-MLH values, (b) expected value of E_{thr} at MAP activation location, and (c) 95% probability volumes related to sampled synthetic MTs. The statistics in the box plots are 25th and 75th percentiles (box), median (red line), outliers (red cross), and maximum and minimum values (whiskers). (d) Evolution of the 95% probability volume with respect to the number of coil configurations using sampled synthetic MTs that result in the maximal MLH at nine configurations.

with the expected value of s and the MAP estimate of r is shown in figure 6(d) for a one sample of $[T_{1,syn}, \ldots, T_{9,syn}]$.

We find that MLH value depends exponentially on the number of coil locations up to seven locations, after which it does not significantly increase. The 95% volume, on the other hand, decreases all the way to ≈ 200 mm³ after each additional coil location. It should be noted that the last coil location introduces quite a lot of variance to the virtual measurement due to its large synthetic measurement value,

possibly explaining the decline of the MLH value after eight locations. The expected value of E_{thr} at the MAP location also appears to tend to its correct value of 65 V m⁻¹, although the variance of the expected value does not decrease, suggesting that the measurement noise sets some lower limit to it.

The 95% probability volume is validated by counting how often the predetermined activation site is included in it. At worst this figure turned out to be 26 out of 30, thus the distribution agrees to the binomial distribution (exact test, $p > 0.06$).
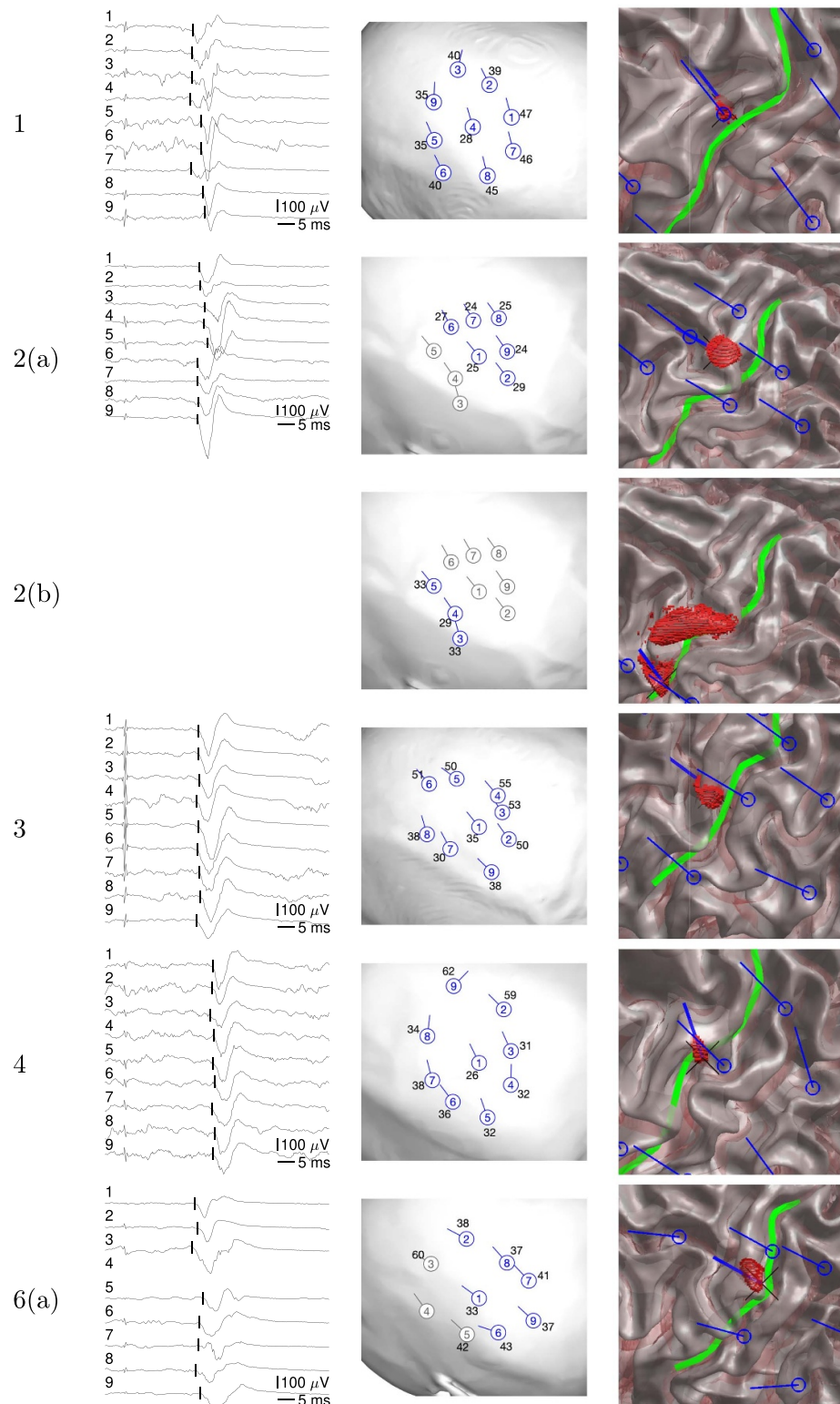
Figure 7. Visual overview of localization measurements and results. The columns (left to right) show the participant number, median of recorded MEP signals whose first negative phase exceeds 100 μV at the threshold intensity for each coil location, the coil locations and directions on scalp and their associated threshold intensities, and overviews of the localization results. Their corresponding legend is in figure 6(d). The second and third rows correspond to two separate activation sites for one participant (see the text). The MT could not be determined for location 4 in participant 6.

4.2. Application to measured data

To test the localization method with real data, we performed TMS experiments and individual electric field modeling in five participants.

Figure 7 displays the median MEP signals, coil locations and thresholds, and visual localization statistics of each participant. The statistics consist of the 95% probability volume, MAP location of r and the expected value of s at that location.
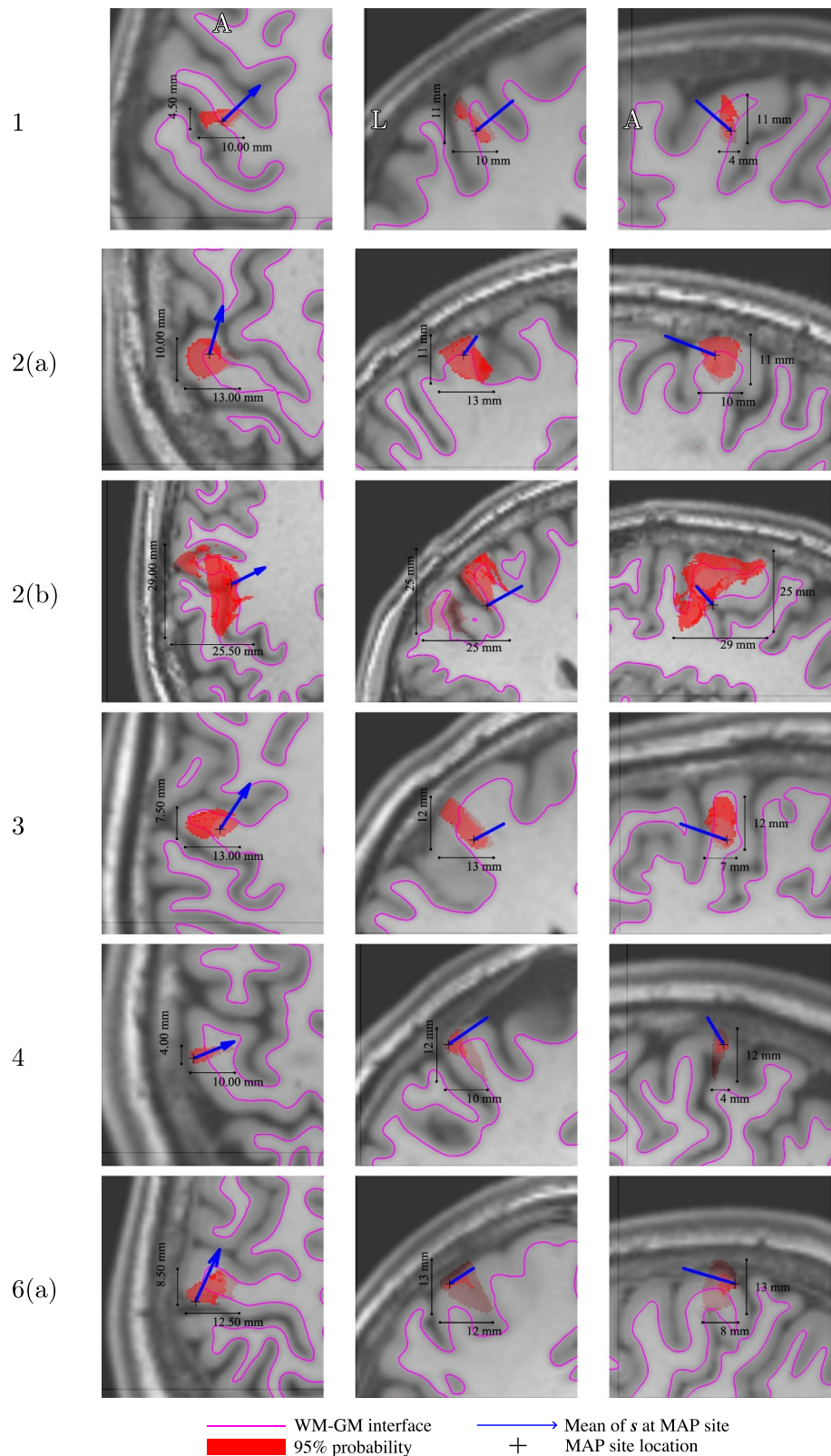
Figure 8. The 95% probability volume parallel-projected over T1-weighted MR-images of axial, coronal and sagittal slices (left to right) intersecting r_{MAP}. Anterior and left direction symbols are overlayed over the first set of images. Note that the MRI slice is rendered in transparent making the part of 95% volume beneath the slice visible.

Further statistics are shown in table 2. In it, the MNI coordinates of the MAP activation site and the expected value of E_{thr} at the MAP site are reported. Also the 95% probability volumes and probabilities of activation site being in white or gray matter, and the associated MLH values are shown.

The MLH values calculated using real data appear to be comparable to those obtained from synthetic

Table 2. Summary of localization results. The data of participant 2 indicated two separate activation sites, which are shown on rows 2(a) and 2(b). The $\mathcal{K}$ values below 0.05 are suffixed with asterisk and are considered to be associated with cases where the measured data does not support the single-site activation model.

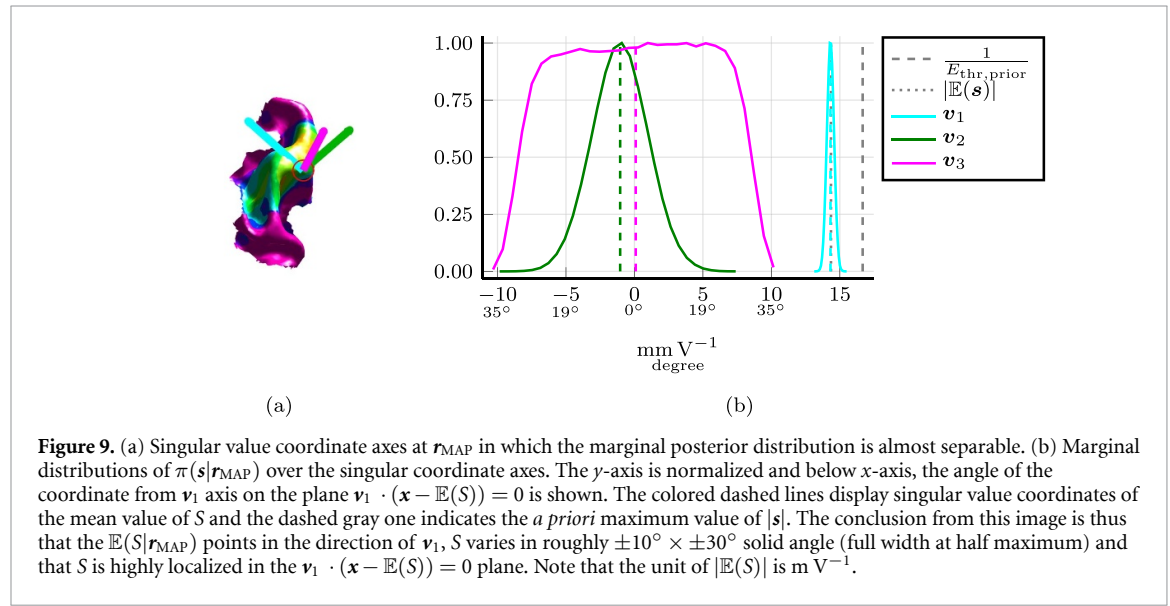| Id	N	MLH	$\mathcal{K}$	CV	Volume (mm^3)	Probability G.M.	Probability W.M.	$\mathbb{E}(E_{\mathrm{thr}})$ (V m^{-1})	MNI x	MNI y	MNI z
1	9	3.27×10^5	0.63	0.07	96	0.681	0.319	64	-38	-13	54
2	9	8.92×10^2	0.00*	0.24							
2(a)	6	1.63×10^5	1.00	0.04	389	0.532	0.468	65	-33	-16	67
2(b)	3	4.17×10^0	0.27	0.09	1305	0.453	0.547	73	-59	-8	39
3	9	5.34×10^4	0.13	0.15	288	0.723	0.277	64	-39	-12	53
4	9	1.74×10^5	0.37	0.07	92	0.161	0.839	70	-44	-16	62
6	8	1.44×10^3	0.03*	0.57							
6(a)	6	1.16×10^3	0.03*	0.04	345	0.448	0.552	64	-39	-25	64

Figure 9. (a) Singular value coordinate axes at $\boldsymbol{r}_{\mathrm{MAP}}$ in which the marginal posterior distribution is almost separable. (b) Marginal distributions of $\pi(\boldsymbol{s}|\boldsymbol{r}_{\mathrm{MAP}})$ over the singular coordinate axes. The y-axis is normalized and below x-axis, the angle of the coordinate from $\boldsymbol{v}_1$ axis on the plane $\boldsymbol{v}_1 \cdot (\boldsymbol{x} - \mathbb{E}(S)) = 0$ is shown. The colored dashed lines display singular value coordinates of the mean value of S and the dashed gray one indicates the *a priori* maximum value of $|\boldsymbol{s}|$. The conclusion from this image is thus that the $\mathbb{E}(S|\boldsymbol{r}_{\mathrm{MAP}})$ points in the direction of $\boldsymbol{v}_1$, S varies in roughly $\pm10° \times \pm30°$ solid angle (full width at half maximum) and that S is highly localized in the $\boldsymbol{v}_1 \cdot (\boldsymbol{x} - \mathbb{E}(S)) = 0$ plane. Note that the unit of $|\mathbb{E}(S)|$ is m V^{-1}.

data, which is indicated by the observation that the synthetically constructed empirical quantile function $\mathcal{K} > 0.05$ at the obtained MLH value. Hence, the single-site activation model seems to be plausible with certain exceptions, which are discussed in the following.

In participant 6, the MLH value is smaller than in other participants and falls to the lower tail of the synthetic MLH distribution with only one virtual measurement producing a smaller MLH value. Hence, while it is certainly possible that equally small MLH values can be produced by chance, no conclusions about the (lack of) plausibility of the model can be drawn due to the limited number of virtual measurements ($n = 30$). However, from the CV RMS value of 0.57 related to this participant we found that the MTs predicted to coil locations 3 and 5 differed from the measured ones much more than those at other locations. Removing these locations (case 6(a) in table 2) improved the CV RMS values significantly while keeping the $\mathcal{K}$ and MLH values largely intact, suggesting that the MTs related coil locations 3 and 5 are due some other activation site or preferred direction. Thus, it appears that high $\mathcal{K}$ values imply low CV RMS score as is shown in table 2, but as evidenced by

the measurements of participant 6 the contrary does not necessarily follow. This could mean that the $\mathcal{K}$ score could be too pessimistic but also that the estimated $\boldsymbol{r}^*$-$\boldsymbol{s}^*$ parameters are good by chance.

In participant 2, an exceptionally small MLH value ($\mathcal{K} = 0$) with nine coil configurations suggest that the single-site-direction activation model is invalid. However, clustering the coil configurations in two sets of $a = \{1, 2, 6, 7, 8, 9\}$ and $b = \{3, 4, 5\}$ result in two much more plausible localizations. This would suggest that the coil locations in these clusters would activate different locations in the brain. The visual statistics of these clusters are shown in figure 7 (second and third row). The 95% probability volumes of the two clusters do not overlap and are found on the opposite edges of the hand knob region. Visual inspection of the MEP latencies in figure 7 for participant 2 shows that the three most lateral coil configurations (3, 4, and 5) have a longer latency than the other six configurations, which further supports the existence of two activation sites.

In all cases the distribution of S given $R = \boldsymbol{r}_{\mathrm{MAP}}$ was largely dictated by the largest singular value of the matrix $\mathbf{TE}$. This can be seen by expressing the conditional distribution $\pi(\boldsymbol{s}|R = \boldsymbol{r}_{\mathrm{MAP}})$ in the singular

value coordinates associated with **TE** and marginalizing two coordinates away at a time resulting in three marginal distributions which summarize the behavior of this conditional distribution.

These marginal distributions and coordinate axes related to participant 4 are displayed in figure 9. From that figure, one can conclude that the S at r_{MAP} is distributed in $\pm 10° \times \pm 30°$ solid angle (full width at half maximum) in a plane defined by a constant first singular value coordinate. In all of the cases, the electric field vectors at r_{MAP} are mostly pointing in the v_1 direction and are scattered in the v_1-v_2 plane. The expectation of S in the singular value coordinates and the norm of it is also shown in the same figure.

5. Discussion

A probabilistic method to infer a cortical activation site associated with MTs of TMS was developed. The method was applied to MEPs measured from the FDI muscle.

The method is based on an elementary cortical activation model, in which an activation at a given location in the brain is considered to occur whenever electric field briefly exceeds, in some preferred direction, a threshold magnitude. The direction, threshold magnitude and location are random variables whose statistics are inferred from measurements. In particular, the MAP estimate and 95% probability volume for the activation site and the expectation of the preferred direction are presented.

An advantage of our approach is that it provides a quantitative estimate of the plausibility of the single-site activation model in terms of the MLH value. This stands in contrast with previous approaches that have employed a similar single-site assumption [7–9, 11]. Exceptionally small MLH values indicate that the hypothesis of a single activation site is not plausible and should be rejected, indicating that there are multiple different activation sites and/or preferred directions (or artefacts that might cause error in the measured thresholds). This occurred in one of our participants, who had a significantly small MLH value. Further investigation showed that there were, in fact, two separate activation sites with different threshold magnitudes and preferred directions. Confirming the model estimates, it also turned out that the latencies of the evoked MEPs were different for the two sites. Approaches that do not estimate the feasibility of the single-site activation model would have possibly indicated an incorrect activation site.

The main contribution to the family of TMS mapping methods is the availability of the marginal probability density function $\pi(r|t)$, from which it is possible to evaluate if the given MAP localization is significantly more probable than the neighboring sites or not, for example. The previous methods, instead, provide some specific correlation type quantity from which the localization is inferred informally—the

MAP location might coincide with other methods but it is not possible to calculate the volumes where the activation occurred with a given probability.

We note that in all the cases, the 95% probability volume derived from the posterior density function intersects the pre-central gyral crown and the anterior wall of the central sulcus rendering it consistent with previous findings [7, 9]. Furthermore, the MNI coordinates of the MAP location are consistent with earlier research [7, 9]. Furthermore, based on these measurements it cannot be ruled out that the activation did not occur in WM as the 95% probability volume clearly intersected WM. Therefore, future TMS localization studies should also include the white matter in the analysis.

It appears that there is a lower limit in how small the 95% probability volume can be. Based on the measurements and the synthetic results, this limit seems to be in the 200 mm^3 range. Adding more coil locations does not translate, after seven or eight locations, in substantially smaller 95% probability volumes. The reason for such a behavior is likely due to the measurement noise. Figure 6(c) provides a rough rule of thumb of how many coil locations are required to achieve certain size for the 95% probability volume.

In the method there is no need to fix the preferred direction of activation $\vec{d}$ *a priori*. Instead, it is just a model parameter to be inferred from the measurements. The findings in five subjects (and six activation sites) showed that the preferred direction is close to being oriented perpendicular to the central sulcus, which is consistent with previous findings that the cortex is most sensitive when the stimulating coil is oriented perpendicular to the sulcus [37, 38]. The reason for existence of, and a motivation in the first place to seek, a preferred direction stems from the observation that neuronal elements in the cortex respond differently depending on the direction of the exciting electric field [39–41]. As the activation site could as well be in the white matter, the directional sensitivity could be also due to the fibre orientation in it [42].

The fibre orientation could also be taken into account in conductivity models of the white matter: differences in the electric field in the white matter as large as 25% have been observed by switching the isotropic conductivity to anisotropic one when the stimulating coil is oriented perpendicular to the gyrus and 40% differences with parallel orientations [43]. By and large, these observations emphasize the importance of the white matter in the localization of the TMS activation sites.

The proposed activation model would suggest that the stimulator threshold t_k should tend to ∞ as the angle θ between the preferred direction and stimulating electric field tends to 90°, which is highly unlikely to occur in practice. However, in addition to multiple activation locations, there could be multiple

preferred directions and thresholds of activation at a single location. Such a hypothesis is supported with computational models of neuronal activation: the threshold is proportional to $\frac{1}{\cos\theta}$ when the electric field is nearly parallel to the preferred direction and taking minimum over multiple such functions with different preferred directions multiplied each with some relative threshold factor, one is expected to obtain threshold maps similar previously reported ones [40, figure 1(D)].

The likelihood of the measurements can be assessed from the MLH values. In the present, we compare the likelihood values to synthetic ones resulting from participant whose brain was imaged and the induced electric field were modeled with the same procedures as the rest of the participants. A more accurate method for finding values for the empirical quantile function $\mathcal{K}$ would be to construct it with the same brain model as the one used in the localization. However, sampling for individualized synthetic MLH values was deemed impractical due to large computational intensity of the method—typically one localization procedure required roughly $4\ldots8\times10^4$ calls for NUTS MCMC sampler each of which evaluating the log-pdf function approximately 10^3 times. Downsampling the electric field to a coarser grid could be used to reduce the computational burden, but the method is still not suitable for Monte Carlo studies.

Granted, just integrating $q(\boldsymbol{r},\boldsymbol{s},\boldsymbol{t})$ with respect to $\boldsymbol{s}$ at each candidate location, would give us the activation site marginal probability distribution, up to multiplicative constant, but finding a reliable quadrature for the integral turned out to be a challenging task. Instead, we chose to use the path sampling technique [20] because it allows controlling the convergence of the integral appearing in (12) in a stable manner: adding more MCMC samples leads to a better approximation of the expectation and adding more integration points to the path results in a better approximation of the integral. However, we believe that the integration can be sped up considerably with some tailored approximation techniques.

The way the MT is inferred from measurements, could be also improved upon. At present, we propose that the threshold electric field at the activation site is equivalent of finding a large enough MEP in the EMG signal in 50% of the stimuli. The drawbacks of such an inference are that it requires relatively large number of stimuli to reliably detect the $\frac{1}{2}$-probability electric field threshold used in the single-site activation model, and the presence of a MEP is defined in a somewhat synthetic fashion (albeit in an accordance to existing best practices [1]): an activation site might reliably elicit a MEPs whose amplitudes were less than $100\ \mu$V. However, the introduction of measurement noise in (4) mitigates these problems as it is actually not necessary to accurately measure the MT.

In conclusion, the presented method for finding the parameters of the described single-site activation model was analyzed and tested, and was found to be a feasible technique for localizing cortical activation sites. Moreover, the single-site activation model is generic and makes very few assumptions on the biophysical activation mechanism of transcranial stimulation allowing the method to be used with any physiological signal for which a threshold can be defined and measured with a known certainty. The proposed approach for finding the activation site builds upon established branch of probability theory, thus improvements of its algorithms, especially ones targeting the integration of marginal distributions, directly translate in improvements to the proposed method. The essential consequence, however, on building upon the probabilistic framework is that the end results of the method are straightforward even for non-experts to analyze.

ORCID iDs

Juhani Kataja ● https://orcid.org/0000-0002-1212-0080
Marco Soldati ● https://orcid.org/0000-0002-2917-320X
Ilkka Laakso ● https://orcid.org/0000-0002-8162-1356

References

[1] Rossini P M *et al* 2015 Non-invasive electrical and magnetic stimulation of the brain, spinal cord, roots and peripheral nerves: basic principles and procedures for routine clinical and research application. an updated report from an I.F.C.N. Committee *Clin. Neurophysiol.* **126** 1071–107

[2] Lefaucheur J-P *et al* 2020 Evidence-based guidelines on the therapeutic use of repetitive transcranial magnetic stimulation (rTMS): an update (2014–2018) *Clin. Neurophysiol.* **131** 474–528

[3] Ilmoniemi R J, Ruohonen J and Karhu J 1999 Transcranial magnetic stimulation–a new tool for functional imaging of the brain *Crit. Rev. Biomed. Eng.* **27** 241–84

[4] Ruohonen J and Karhu J 2010 Navigated transcranial magnetic stimulation *Neurophysiol. Clin./Clin. Neurophysiol.* **40** 7–17

[5] Opitz A, Legon W, Rowlands A, Bickel W K, Paulus W and Tyler W J 2013 Physiological observations validate finite element models for estimating subject-specific electric field distributions induced by transcranial magnetic stimulation of the human motor cortex *Neuroimage* **81** 253–64

[6] Opitz A, Zafar N, Bockermann V, Rohde V and Paulus W 2014 Validating computationally predicted TMS stimulation areas using direct electrical stimulation in patients with brain tumors near precentral regions *Neuroimage Clin.* **4** 500–7

[7] Bungert A, Antunes A, Espenhahn S and Thielscher A 2016 Where does TMS stimulate the motor cortex? Combining electrophysiological measurements and realistic field

estimates to reveal the affected cortex position *Cereb. Cortex* **27** 5083–94

[8] Thielscher A and Kammer T 2002 Linking physics with physiology in TMS: a sphere field model to determine the cortical stimulation site in TMS *Neuroimage* **17** 1117–30

[9] Laakso I, Murakami T, Hirata A and Ugawa Y 2018 Where and what TMS activates: experiments and modeling *Brain Stimul.* **11** 166–74

[10] Aonuma S, Gomez-Tames J, Laakso I, Hirata A, Takakura T, Tamura M and Muragaki Y 2018 A high-resolution computational localization method for transcranial magnetic stimulation mapping *Neuroimage* **172** 85–93

[11] Weise K, Numssen O, Thielscher A, Hartwigsen G and 2020 Thomas R Knösche. A novel approach to localize cortical TMS effects *Neuroimage* **209** 116486

[12] Wang W and Eisenberg S R 1994 A three-dimensional finite element method for computing magnetically induced currents in tissues *IEEE. T. Magn.* **30** 5015–23

[13] Braess D 2001 Theory, fast solvers and applications in solid mechanics, translated from the 1992 *Finite Elements* 2nd edn, ed L L Schumaker (Cambridge: Cambridge University Press)

[14] Laakso I and Hirata A 2012 Fast multigrid-based computation of the induced electric field for transcranial magnetic stimulation *Phys. Med. Biol.* **57** 7753–65

[15] Çan M K, Laakso I, Nieminen J O, Murakami T and Ugawa Y 2018 Coil model comparison for cerebellar transcranial magnetic stimulation *Biomed. Phys. Eng. Express* **5** 1

[16] Aberra A S, Peterchev A V and Grill W M 2018 Biophysically realistic neuron models for simulation of cortical stimulation *J. Neural Eng.* **15** 066023

[17] Soldati M, Mikkonen M, Laakso I, Murakami T, Ugawa Y and Hirata A 2018 A multi-scale computational approach based on TMS experiments for the assessment of electro-stimulation thresholds of the brain at intermediate frequencies *Phys. Med. Biol.* **63** 225006

[18] Kaipio J and Somersalo E 2004 *Statistical and Computational Inverse Problems* (New York: Springer)

[19] Diekhoff S, Uludağ K, Sparing R, Tittgemeyer M, Cavuşoğlu M, von Cramon D Y and Grefkes C 2011 Functional localization in the human brain: gradient-echo, spin-echo and arterial spin-labeling fMRI compared with neuronavigated TMS *Human Brain Mapp.* **32** 341–57

[20] Gelman A and Meng X-Li 1998 Simulating normalizing constants: from importance sampling to bridge sampling to path sampling *Stat. Sci.* **13** 163–85

[21] Hoffman M D and Gelman A 2011 The No-U-Turn Sampler: Adaptively Setting Path Lengths in Hamiltonian Monte Carlo 1111.4246

[22] Kai X, Tebbutt W, Trapp M and Ghahramani Z 2020 AdvancedHMC. jl: A robust, modular and efficient implementation of advanced HMC algorithms *Symposium on Advances in Approximate Bayesian Inference* 1–10

[23] Dale A M, Fischl B and Sereno M I 1999 Cortical surface-based analysis. i. Segmentation and surface reconstruction *Neuroimage* **9** 179–94

[24] Fischl B, Sereno M I, Tootell R B and Dale A M 1999 High-resolution intersubject averaging and a coordinate system for the cortical surface *Human Brain Mapp.* **8** 272–84

[25] Laakso I, Tanaka S, Koyama S, Valerio D S and Hirata A 2015 Inter-subject variability in electric fields of motor cortical tDCS *Brain Stimul.* **8** 906–13

[26] Koessler L, Colnat-Coulbois S, Cecchin T, Hofmanis J, Dmochowski J P, Norcia A M and Maillard L G 2017 In-vivo measurements of human brain tissue conductivity using focal electrical current injection through intracerebral multicontact electrodes *Human Brain Mapp.* **38** 974–86

[27] Gabriel S, Lau R W and Gabriel C 1996 The dielectric properties of biological tissues: III. Parametric models for the dielectric spectrum of tissues *Phys. Med. Biol.* **41** 2271–93

[28] Fonov V S, Evans A C, McKinstry R C, Almli C R and Collins D L 2009 Unbiased nonlinear average age-appropriate brain templates from birth to adulthood *Neuroimage* **47** S102

[29] Vladimir Fonov A C Evans K B, Robert Almli C, McKinstry R C, Louis Collins D and Brain Development Cooperative Group 2011 Unbiased average age-appropriate atlases for pediatric studies *Neuroimage* **54** 313–27

[30] Baumann S B, Wozny D R, Kelly S K and Meno F M 1997 The electrical conductivity of human cerebrospinal fluid at body temperature *IEEE Trans. Biomed. Eng.* **44** 220–3

[31] Akhtari M *et al* 2002 Conductivities of three-layer live human skull *Brain Topography* **14** 151–67

[32] Wake K, Sasaki K and Watanabe S 2016 Conductivities of epidermis, dermis and subcutaneous tissue at intermediate frequencies *Phys. Med. Biol.* **61** 4376

[33] Gabriel C, Peyman A and Grant E H 2009 Electrical conductivity of tissue at frequencies below 1 MHz *Phys. Med. Biol.* **54** 4863–78

[34] Gabriel S, Lau R W and Gabriel C 1996 The dielectric properties of biological tissues: II. Measurements in the frequency range 10 Hz to 20 GHz *Phys. Med. Biol.* **41** 2251–69

[35] Geddes L A and Baker L E 1967 The specific resistance of biological material–a compendium of data for the biomedical engineer and physiologist *Med. Biol. Eng.* **5** 271–93

[36] Stoy R D, Foster K R and Schwan H P 1982 Dielectric properties of mammalian tissues from 0.1 to 100 mHz: a summary of recent data *Phys. Med. Biol.* **27** 501–13

[37] Mills K R, Boniface S J and Schubert M 1992 Magnetic brain stimulation with a double coil: the importance of coil orientation *Electroencephalogr. Clin. Neurophysiol.* **85** 17–21

[38] Brasil-Neto J P, Cohen L G, Panizza M, Nilsson J, Roth B J and Hallett M 1992 Optimal focal transcranial magnetic activation of the human motor cortex: effects of coil orientation, shape of the induced current pulse and stimulus intensity *J. Clin. Neurophysiol.* **9** 132–6

[39] Gomez-Tames J, Laakso I, Murakami T, Ugawa Y and Hirata A 2020 TMS activation site estimation using multiscale realistic head models *J. Neural Eng.* **17** 036004

[40] Aberra A S, Wang B, Grill W M and Peterchev A V 2020 Simulation of transcranial magnetic stimulation in head model with morphologically-realistic cortical neurons *Brain Stimul.* **13** 175–89

[41] Seo H, Schaworonkow N, Jun S C and Triesch J 2017 A multi-scale computational model of the effects of TMS on motor cortex *F1000Research* **5** 1945

[42] Herbsman T *et al* 2009 Motor threshold in transcranial magnetic stimulation: the impact of white matter fiber orientation and skull-to-cortex distance *Human Brain Mapp.* **30** 2044–55

[43] Opitz A, Mirko Windhoff R M Heidemann R T and Thielscher A 2011 How the brain tissue shapes the electric field induced by transcranial magnetic stimulation *Neuroimage* **58** 849–59